RSC Advances

ROYAL SOCIETY OF CHEMISTRY

PAPER

View Article Online
View Journal | View Issue

Check for updates

Cite this: *RSC Adv.*, 2025, **15**, 48226

Surface-cleaned hydroxyapatite nanowires for aqueous copper ion removal: performance, adsorption mechanisms and membrane filtration application

Yuwei Jiang, Shuang Zhang, Jie Li and Junjun Tan *

Received 18th August 2025
Accepted 1st December 2025

DOI: 10.1039/d5ra06089c

rsc.li/rsc-advances

Ligand-assisted nanoparticle synthesis offers precise size and morphology control but often compromises intrinsic surface properties and hinders further functionalization due to ligand capping. To address this limitation, we demonstrate a simple and efficient strategy for complete ligand removal using oleate-capped hydroxyapatite (HA) nanowires as a model system. Ethanol treatment at 70 °C (denoted ET-70) effectively eliminates oleate ligands from HA nanowire surfaces, as confirmed by FTIR and contact angle analyses. The resulting clean surfaces expose abundant active sites, significantly enhancing copper ion adsorption capacity compared to untreated counterparts. Batch adsorption experiments demonstrated that ET-70 achieved a maximum Cu^{2+} adsorption capacity of 63.92 mg g^{-1} with a removal efficiency of 12.79% at an initial concentration of 200 mg L^{-1} and 45 °C. The adsorption process was well-described by the Langmuir isotherm and pseudo-second-order kinetic models. Remarkably, ET-70 maintained high removal efficiency across wide pH ranges and in the presence of coexisting ions. In membrane filtration applications, HA nanowire membranes processed 197.95 L m^{-2} of copper-contaminated water (influent: 5 mg L^{-1} Cu^{2+}, flow rate: 0.95 mL min^{-1}) while consistently meeting the WHO safety standard (<2 mg L^{-1} effluent concentration). Mechanistic studies indicate that adsorption primarily occurs through ion exchange between Ca^{2+} in HA and Cu^{2+} in solution, complemented by surface complexation with hydroxyl groups. This work not only establishes a versatile ligand-removal protocol for unlocking the functional potential of surfactant-capped nanomaterials but also provides foundational insights for implementing HA nanowires in practical water purification technologies.

1 Introduction

Hydroxyapatite ($Ca_{10}(PO_4)_6(OH)_2$, HA), the primary inorganic constituent of vertebrate bones and teeth,[1,2] possesses exceptional biocompatibility, bioactivity, and ion-exchange capacity. These properties underpin its extensive use in biomedical applications such as bone regeneration,[3,4] drug delivery,[5,6] and critically, environmental remediation through heavy metal ion adsorption.[7] The effectiveness of HA in adsorbing toxic metals such as copper ions depends on its morphology and surface properties.

To achieve precise morphological control over HA nanoparticles, various synthetic strategies including hydrothermal,[8,9] microwave-assisted,[10,11] and sol–gel methods[12] have been developed. Among these, oleic acid (OA)-assisted hydrothermal synthesis stands out for its unparalleled ability to generate HA nanostructures with uniform morphology, narrow size distribution, and exceptional aspect ratio tunability (1 to >10 000).[13–16] By modulating key parameters such as hydrothermal temperature, reaction duration, and phosphate source, this method enables the tailored production of HA nanocrystals ranging from nanoparticles to ultralong nanowires.

However, a fundamental limitation persists: OA-mediated synthesis necessitates sodium oleate, resulting in nanocrystals coated with a tenacious oleate layer. This confers hydrophobicity, facilitating dispersion in organic solvents (*e.g.*, toluene, cyclohexane) but severely impeding aqueous dispersibility. Consequently, the adsorbed OA sterically blocks reactive surface sites (*e.g.*, Ca^{2+}, PO_4^{3-}, OH^-) and inhibits interaction with aqueous contaminants, drastically restricting HA's utility in water-based heavy metal adsorption.

Previous attempts to address this include: OA removal *via* aggressive base/ethanol hydrothermal treatments,[17] calcination treatment,[18] Surface functionalization with silica coatings,[19] polymeric encapsulation using amphiphilic surfactants[6] and ligand exchange with sodium citrate.[20] While partially effective, these strategies often compromise nanocrystal morphology,

---

Hubei Provincial Key Laboratory of Green Materials for Light Industry, School of Materials and Chemical Engineering, Hubei University of Technology, Wuhan, 430068, China. E-mail: tanjunjun2011@hbut.edu.cn; Fax: +86 27 59750482; Tel: +86 27 59750460

introduce non-native coatings, or fail to restore intrinsic surface reactivity.

Herein, we propose a targeted solution: a mild yet efficient thermal ethanol treatment to selectively remove the OA layer from oleate-capped HA nanowires while preserving their anisotropic morphology and crystallinity. This approach leverages ethanol's capacity to solubilize OA without degrading the HA structure. By eliminating the hydrophobic barrier, we expose native surface sites and hydroxyl groups, thereby unlocking the full ion-exchange potential of HA. We demonstrate that OA-free HA nanowires exhibit superior aqueous dispersibility and dramatically enhanced adsorption capacity for Cu^{2+} ions—a critical pollutant in industrial wastewater. This strategy bridges the gap between high-precision HA nanostructure synthesis and practical environmental application, offering a scalable pathway for advanced water purification technologies.

2 Materials and methods

2.1 Materials

Calcium chloride dihydrate ($CaCl_2 \cdot 2H_2O$, ≥99.0%), monometallic sodium orthophosphate ($Na_2HPO_4 \cdot 12H_2O$, ≥98.0%), oleic acid ($C_{18}H_{34}O_2$, ≥99.0%), anhydrous ethanol (C_2H_6O, ≥99.7%), sodium hydroxide (NaOH, ≥97.0%), were obtained from Shanghai Aladdin Reagent Co. (Shanghai, China). Nitric acid (HNO_3, ≥68%) were obtained from Sinopharm Chemical Reagent Co. The chemical reagents involved throughout the study were used directly without further purification, and the water involved in the use was deionized water.

2.2 Preparation of the HA nanowires coated with oleic acid

In a typical synthesis, 11.29 g of oleic acid and 6 g of ethanol were co-mixed for five minutes in a 250 mL beaker. First, an aqueous NaOH solution (1.2 g, 15 g water) was added to the mixture with a peristaltic pump at 4.5 rpm and remained stirred for 10 minutes after the addition was completed. Then, an aqueous $CaCl_2$ solution (0.5880 g, 15 g water) was added to the mixture with a peristaltic pump at 4.5 rpm and remained stirred for 10 minutes after the addition was completed. After that, an aqueous Na_2HPO_4 solution (1.146 g, 15 g water) was added to the mixture with a peristaltic pump at 4.5 rpm and remained stirred for 20 minutes after the addition was completed.

Finally, the mixture was transferred to a Teflon lined hydrothermal autoclave and placed in an oven for hydrothermal treatment with a hydrothermal temperature of 180° and a hydrothermal time of 24 hours. After completion of the hydrothermal treatment, the hydrothermal autoclave was cooled to room temperature and the product was purified by a three-round centrifugation-wash process with water and ethanol. Finally, the remaining product was dried in an oven at 80 °C for 24 h to obtain the powder for future characterization.

2.3 "Clean" the oleic acid molecules adsorption on the HA nanowires

A mixture of 0.4 g of the purified product and 40 g of ethanol was prepared in a 100 mL single-neck flask. The mixture was heated to specific temperatures (30, 40, 50, 60 and 70 °C, respectively) under magnetic stirring and maintained for 30 minutes. Afterward, it was cooled to room temperature and centrifuged. This process was repeated three times. The separated solid product was dried in an oven (80 °C, 24 h) to obtain the final powder.

2.4 Preparation of the HA nanowires membrane

The HA nanowire membrane was typically prepared as follows. First, powdered HA nanowires were dispersed into water under continuous stirring for 10 minutes. The resulting dispersion was then poured onto filter paper placed in a Buchner funnel. Under vacuum suction, a white HA nanowire membrane formed on the filter paper. Finally, the membrane was easily detached from the filter paper using tweezers.

2.5 Characterization

X-ray diffraction (XRD) patterns were acquired using a Bruker D8 Advance diffractometer (Bruker AXS, Karlsruhe, Germany) with Cu Kα radiation ($\lambda = 0.15406$ nm). Scans were performed over the 2θ range of 5° to 80° at a scan rate of 6° min^{-1}. Field-emission scanning electron microscopy (FE-SEM) was conducted on a Hitachi SU-8010 microscope (Hitachi High Technologies, Japan). Samples were sputter-coated with gold for 30 s using an MSP-2S magnetron coater prior to imaging. Zeta potential measurements were performed on a Zetasizer Nano ZS90 (Malvern Instruments Ltd, UK). Sample pH was adjusted with 0.1 M NaOH or 0.1 M HCl and verified using a Sartorius PB-10 pH meter at 25 °C. Measurements were conducted without added electrolytes. Data were processed using Dispersion Technology Software v. 5.0 (Malvern Instruments). X-ray photoelectron spectroscopy (XPS) analysis was carried out on a Thermo Scientific ESCALAB 250Xi spectrometer with Al Kα radiation. Nitrogen adsorption–desorption isotherms were measured at 77 K using a 3Flex surface analyzer (Micromeritics Instrument Corp., USA). Specific surface areas were calculated by the Brunauer–Emmett–Teller (BET) method, while pore size distributions were derived from desorption branches using the Barrett–Joyner–Halenda (BJH) model. Fourier-transform infrared (FTIR) spectra were recorded on a Nicolet iS5 spectrometer (400–4000 cm^{-1}) using KBr pellet preparations.

2.6 Batch adsorption experiments

In order to evaluate the adsorption performance of the prepared adsorbent on copper ions in water, batch adsorption experiments were carried out. The adsorption isotherm was measured at a pH of 5.5 and an adsorbent addition of 0.4 g L^{-1} 10 mg of adsorbent was added to a polyethylene centrifuge tube containing 25 mL of a specific concentration of copper(II) nitrate test solution (10 to 200 mg L^{-1}) and then the flasks were shaken at 100 rpm in a shaker at three different temperatures, *viz.*, 25, 35 and 45 °C for 24 hours to reach adsorption equilibrium. After completion of adsorption, the solution was centrifuged at 8000 rpm for 5 minutes and its supernatant was used by a UV-vis spectrophotometer (UV-Mini 1280, Shimadzu, Japan) for determination of copper ion concentration. The relationship between the copper ion standard solution concentration and the absorbance values is shown in Fig. S1.

All measurements were carried out at 25 °C and the adsorption capacity (q_e, mg g^{-1}) was calculated according to the following equation:[21]

$$q_e = \frac{(C_0 - C_e)V}{m} \tag{1}$$

where C_0 and C_e are the initial concentration and equilibrium concentrations (mg L^{-1}) of Cu^{2+} ions in solution, respectively, V is the volume of Cu^{2+} ions solution (Liter), and m is the mass of adsorbent added (gram).

2.6.1 Adsorption kinetics. Batch experiments were conducted in polyethylene centrifuge tubes containing 100 mg L^{-1} Cu^{2+} solution. Each tube received 10 mg of adsorbent and was immediately agitated in a constant-temperature shaker (100 rpm, 25 °C). After predetermined contact times, suspensions were centrifuged and the supernatant Cu^{2+} concentration was quantified.

2.6.2 Adsorption isotherms. Solutions with varying initial Cu^{2+} concentrations were prepared in polyethylene centrifuge tubes. Following addition of 10 mg adsorbent to each tube, samples were shaken (100 rpm) for 24 h to reach equilibrium at different temperature. Separation was achieved by centrifugation prior to measurement of equilibrium Cu^{2+} concentration in the supernatant.

2.6.3 Effect of initial pH. The influence of solution pH (3.0–5.5) on adsorption performance was evaluated using 0.1 M HNO_3 or 0.1 M NaOH for pH adjustment. Experiments employed 10 mg L^{-1} Cu^{2+} solutions with 0.4 g L^{-1} adsorbent dosage, shaken for 24 h at 25 °C.

2.6.4 Effect of coexisting ions. Competitive adsorption studies introduced coexisting anions (Na^+, K^+, Mg^{2+}, Ca^{2+}) at concentrations of 0.1, 0.3, 0.6, and 1.0 mM to 10 mg L^{-1} Cu^{2+} solutions. All tests used 0.4 g L^{-1} adsorbent dosage under standardized conditions.

2.7 Membrane filtration experiments

A filtration setup was assembled to evaluate the Cu^{2+} removal efficiency of the HA nanowire membrane. The membrane disc (diameter: 2.5 cm; thickness: 0.15 mm) had a mass of 0.0313 g. Cu^{2+} solutions were pumped through the HA nanowire membrane using a peristaltic pump. During filtration, Cu^{2+} were captured *via* adsorption onto the HA nanowires as the solution permeated the membrane. The effects of two key operational parameters on membrane adsorption performance were systematically investigated: flow rate and initial Cu^{2+} concentration of the solution.

3 Results and discussion

3.1 HA nanowires with ethanol treatment at different temperatures

Fig. 1a illustrates the three-step synthesis strategy: (1) hydrothermal treatment of calcium ions, phosphate ions, and oleic acid in a water/ethanol cosolvent yields HA nanowires. (2) Purification removes excess oleic acid and electrolytes, resulting in HA nanowires coated with a monolayer of oleic acid. (3) Stirring the oleic acid-coated HA nanowires in ethanol at a specific temperature for a defined duration, followed by centrifugation, produces HA nanowires with a "clean" (ligand-free) surface. Fig. 1b shows the copper removal efficiency of ethanol-treated HA nanowires at different temperatures (Adsorbent dosage: 0.4 g L^{-1}; adsorption time: 24 h; initial pH: 5.5; C_0: 10 mg L^{-1}). Untreated HA nanowires achieved only 28.09% copper removal efficiency. In contrast, ethanol treatment significantly enhanced efficiency, reaching 96.21% at 70 °C. This demonstrates that ethanol treatment, particularly at 70 °C, markedly improves the copper removal capacity of HA nanowires. Fig. 1c presents the FTIR spectra of HA nanowires. Untreated nanowires exhibited characteristic HA absorption bands: phosphate vibrations at 564, 605, 1035, and 1096 cm^{-1}, and an O–H stretch at 3573 cm^{-1}. They also displayed distinct oleic acid bands: carboxylate ($-COO^-$) vibrations at 1410, 1459, and 1552 cm^{-1}, and C–H stretches at 2922 and 2952 cm^{-1}, confirming oleic acid capping on the HA surface. After ethanol treatment, the C–H (2922, 2952 cm^{-1}) and carboxylate (1552–1591 cm^{-1}) bands disappeared, indicating complete removal of the oleic acid ligands. Fig. 1d compares the XRD patterns of HA nanowires before and after ethanol treatment. Both samples show diffraction peaks at 26.0° (002), 32.1° (211), 34.1° (202), 39.9° (310), 46.8° (222), 49.6° (213), 53.3° (004), and 64.1° (304), consistent with hexagonal HA (JCPDS No. 09-0432).[9] The sharp, well-defined peaks indicate high crystallinity. The similarity in patterns before and after treatment confirms that ethanol treatment does not alter the crystallinity or phase purity of the HA nanowires. Fig. 1e shows the contact angles of HA nanowire powders. The contact angle decreased from 118.3° (untreated) to 28.3° after ethanol treatment at 70 °C, demonstrating a transition from hydrophobic to hydrophilic surface properties. Fig. 1f presents the BET analysis of sample ET-70 dry powders. Nitrogen adsorption–desorption isotherms for all samples exhibited characteristic type IV profiles with H4-type hysteresis loops, indicative of mesoporous structures possessing slit-shaped pores. Sample ET-70 exhibited a specific surface area of 52.74 m^2 g^{-1} and an average pore size of 22.54 nm. The corresponding pore size distribution curve further confirms the mesoporous nature of the material. Fig. 1g shows a representative SEM image of the sample ET-70. Its nanowires display a flexible wire-like morphology, with average particle dimensions of 119 μm in length and 18 nm in diameter.

3.2 Cu^{2+} adsorption performance of the sample ET-70

3.2.1 Adsorption of time dependence. Fig. 2a shows the adsorption kinetics of the sample ET-70. The adsorption capacity of sample ET-70 increased rapidly within the first 120 min, approaching equilibrium by 200 min. To elucidate the adsorption kinetics of Cu^{2+} removal, the experimental data were fitted to pseudo-first-order and pseudo-second-order kinetic models.[22–24] The forms of these models are given by:

Pseudo-first-order:

$$q_t = q_e\,(1 - e^{-k_1 t}) \tag{4}$$

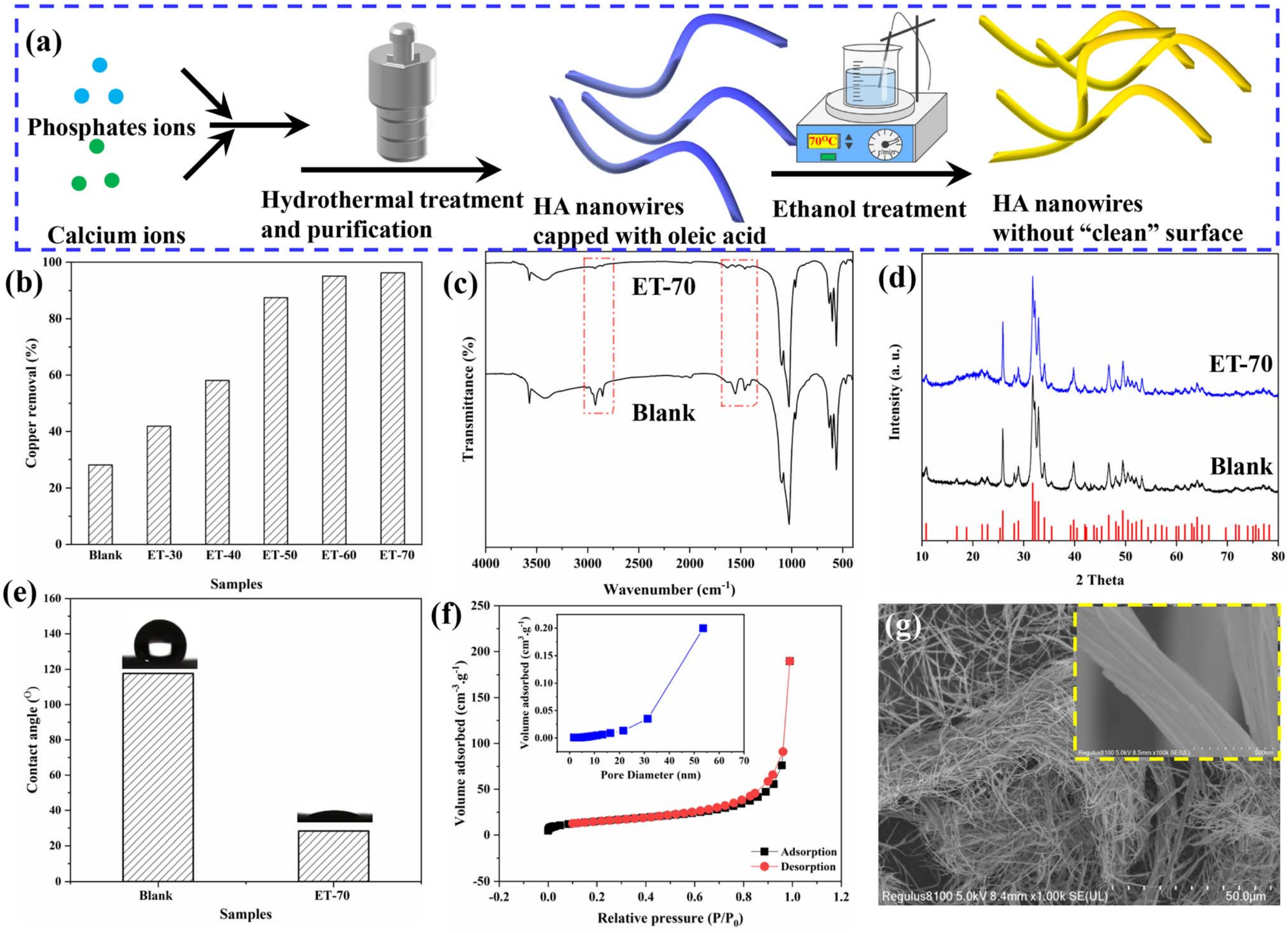

Fig. 1 (a) Schematic illustration of sample preparation; (b) copper removal efficiency, (c) FTIR spectra, (d) XRD patterns, and (e) contact angle of HA nanowires with ethanol treatment at different temperatures; (f) BET surface area and (g) SEM image of the HA nanowires with ethanol treatment at 70 °C.

Pseudo-second-order:

$$\frac{t}{q_t} = \frac{1}{k_2 {q_e}^2} + \frac{t}{q_e} \tag{5}$$

where: q_t is the adsorption capacity (mg g^{-1}) at time "t"; q_e is the equilibrium adsorption capacity (mg g^{-1}); k_1 is the pseudo-first-order rate constant (min^{-1}); k_2 is the pseudo-second-order rate constant (g mg^{-1} min^{-1}).

The fitting results for both models are presented in Fig. 2b (pseudo-first-order) and Fig. 2c (pseudo-second-order), with corresponding parameters summarized in Table 1. The pseudo-first-order model yielded a theoretical q_e value of 55.30 mg g^{-1} for sample ET-70, while the pseudo-second-order model gave an identical theoretical q_e of 58.51 mg g^{-1}. However, comparison of the correlation coefficients (R^2) revealed superior fit for the pseudo-second-order model (R^2 = 0.974 for pseudo-first-order

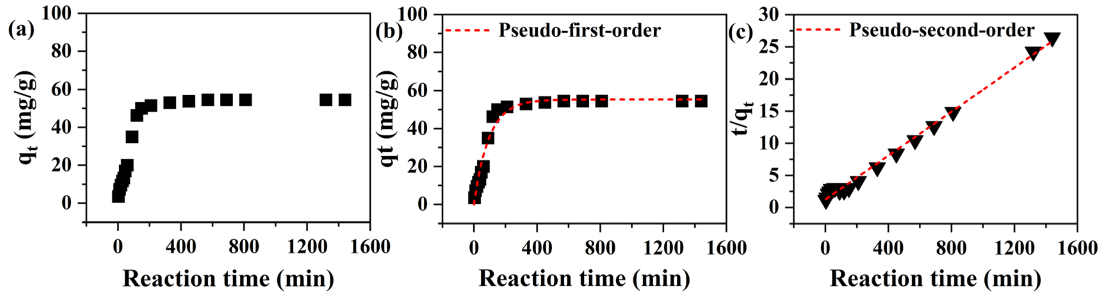

Fig. 2 Adsorption kinetics of Cu^{2+} ions on sample ET-70 (a), non-linear fitting of adsorption kinetics: pseudo-first-order model (b), linear fitting of adsorption kinetics: pseudo-second-order model (c). Experimental conditions: adsorbent dose = 0.4 g L^{-1}, pH = 5.5, T = 25 °C and C_0 = 100 mg L^{-1}.

Table 1 Kinetic parameters for copper adsorption on the prepared samples, derived from pseudo-first-order and pseudo-second-order models

	Pseudo-first-order model			Pseudo-second-order model		
Samples	q_e (mg g^{-1})	k_1 (1 min^{-1})	R^2	q_e (mg g^{-1})	k_2 (g mg^{-1} min^{-1})	R^2
ET-70	55.30	0.010	0.974	58.51	0.24	0.994

vs. 0.994 for pseudo-second-order), indicating this model better describes the adsorption kinetics.

3.2.2 Adsorption of temperature dependence. To evaluate the adsorption capacity of the samples, adsorption isotherm experiments were conducted at varying C_0 [Cu^{2+}] (Fig. 3a). The experimental data were linearly fitted using the Langmuir (Fig. 3b) and Freundlich (Fig. 3c) models. The corresponding parameters derived from these fits are summarized in Table 2.

The linearized forms of the isotherm models are given by:[25]

Langmuir model:

$$\frac{C_e}{q_e} = \frac{1}{K_L q_m} + \frac{C_e}{q_m} \tag{2}$$

Freundlich model:

$$\ln q_e = \ln K_F + \frac{1}{n}\ln C_e \tag{3}$$

where: q_e is the equilibrium adsorption capacity (mg g^{-1}); C_e is the equilibrium Cu^{2+} concentration (mg L^{-1}); q_m is the theoretical maximum monolayer adsorption capacity (mg g^{-1}); K_L is the Langmuir constant related to adsorption affinity (L mg^{-1}); K_F is the Freundlich constant indicative of adsorption capacity ((mg g^{-1}) (L mg^{-1})$^{1/n}$); $1/n$ is the Freundlich exponent related to adsorption intensity or surface heterogeneity.

Comparison of the correlation coefficients (R^2) revealed that the adsorption behavior of the samples aligned more closely with the Langmuir model than the Freundlich model. This suggests a predominantly monolayer adsorption mechanism occurring on a homogeneous surface. Furthermore, the equilibrium adsorption capacity increased with both increasing temperature and higher initial copper ion concentrations. The Langmuir model yielded a maximum adsorption capacity of 62.97 mg g^{-1} for the sample ET-70 under conditions of 200 mg L^{-1} initial Cu^{2+} concentration and 45 °C.

For comparison, the maximum adsorption capacities of copper ions on various HA-related adsorbents are summarized in Table 3. As evident from the data, sample ET-70 exhibits a relatively high adsorption capacity compared to most adsorbents reported in the literature. This indicates that ET-70 demonstrates potential for copper removal in wastewater.

3.2.3 Adsorption thermodynamic parameters analysis. The thermodynamic nature of an adsorption process—whether endothermic or exothermic, spontaneous or non-spontaneous—can be assessed by determining key parameters: the standard Gibbs free energy change ($\Delta G°$), standard enthalpy change ($\Delta H°$), and standard entropy change ($\Delta S°$). These parameters were derived from adsorption isotherm data obtained at different temperatures.

The standard Gibbs free energy change ($\Delta G°$) was calculated using:

$$\Delta G^{\circ} = -RT\ln K^{0} \tag{6}$$

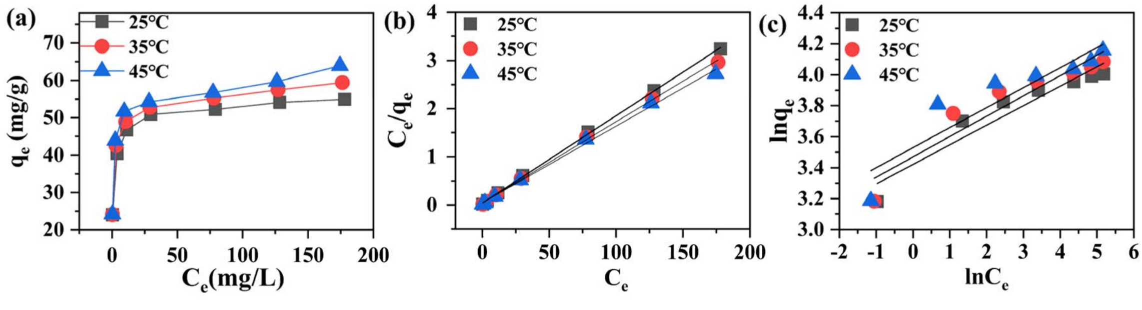

Fig. 3 Adsorption isotherms of Cu^{2+} ions on sample HA-ET-70 (a). Linear fitting of adsorption isotherms: Langmuir model (b); Freundlich model (c). Experimental conditions: adsorbent dose = 0.4 g L^{-1}, adsorption time = 24 h, pH = 5.5, and C_0 = 10–200 mg L^{-1}.

Table 2 Adsorption parameters for copper adsorption on the prepared samples, calculated using Langmuir and Freundlich isotherm models

		Langmuir isotherm				Freundlich isotherm		
Adsorbents	Temperature (°C)	$q_{m(cal)}$ (mg g^{-1})	$q_{m(exp)}$ (mg g^{-1})	K_L (L mg^{-1})	R^2	K_F (mg g^{-1})/(mg L^{-1})^n	n	R^2
ET-70	25	55.16	54.92	0.448	0.999	30.62	7.92	0.913
	35	59.31	59.42	0.407	0.998	32.14	7.62	0.892
	45	62.97	63.93	0.336	0.996	34.11	7.74	0.813

Table 3 Comparison of copper ion adsorption properties on various adsorbents[a]

Adsorbents	pH	q_m (mg g^{-1})	References
ET-70	5.5	63.93	This work
Humic acid modified HA nanoparticles	5.5	58.42	26
HA/biochar nanocomposites	5.0	99.01	27
Hydroxyapatite-*in situ* self-doped fluffy biochar	5.0	79.68	28
Hydroxyapatite modified sludge-based biochar	6.0	89.17	23
HA incorporated gelatin/zein nanofibrous membranes	—	67.80	29
HA-alginate nanocomposite	—	60.99	30
Biogenic HA	5.0	82.05	31
HA from pig-bone waste	7.0	50.25	32
Natural HA from fishbone waste	6.0	24.09	33
HA derived from flue gas desulphurization gypsum	6.0	29.23	34

[a] The key innovation of ET-70 is its capability to bridge the gap between high adsorption performance and practical application. While achieving a high adsorption capacity, its ultralong nanowire morphology allows it to be fabricated into robust filters for dynamic flow-through systems, a critical advancement towards the practical deployment of hydroxyapatite-based materials in continuous wastewater remediation.

Table 4 Thermodynamic parameters for the adsorption of copper ions from aqueous solution by the sample ET-70

Adsorbent	Temp. (K)	ΔG (kJ mol^{-1})	ΔH (kJ mol^{-1})	ΔS (J mol^{-1} K^{-1})
ET-70	298	−5.65	13.00	62.60
	308	−6.28		
	318	−6.91		

where: K^0 is the thermodynamic equilibrium constant (L g^{-1}); T is the absolute temperature (K); R is the ideal gas constant (8.314 J mol^{-1} K^{-1}).

The value of $\ln K^0$ was determined by plotting $\ln K_d$ (where the distribution coefficient $K_d = q_e/C_e$) against C_e and extrapolating to $C_e \to 0$ (Fig. S2). The y-intercept of this plot corresponds to $\ln K^0$.

The standard enthalpy change (ΔH°) and standard entropy change (ΔS°) were obtained from the van't Hoff equation:

$$\ln K^0 = -\Delta H^\circ/(RT) + \Delta S^\circ/R \tag{7}$$

A linear plot of $\ln K^0$ *versus* $1/T$ (Fig. S2) yielded these parameters from the slope and intercept, respectively.

Table 4 summarizes the calculated thermodynamic parameters for copper adsorption on the samples. For sample ET-70, the positive ΔH° values confirm the adsorption process is endothermic, requiring energy input. The negative ΔG° values indicate the process is spontaneous under the experimental conditions. The decrease in ΔG° (becoming less negative) with rising temperature indicates increased spontaneity at higher temperatures. This suggests higher temperatures provide a stronger thermodynamic driving force for adsorption.

3.2.4 Adsorption mechanism. In order to reveal the adsorption mechanism of ET-70, the XPS, zeta potential and pH variation of sample was conducted. Fig. 4a shows the XPS survey scans of the sample ET-70 before and after adsorption. While pristine HA exhibited dominant Ca 2p, P 2p, and O 1s peaks, post-adsorption samples showed new characteristic Cu 2p$_{3/2}$ and Cu 2p$_{1/2}$ peaks at 930–955 eV, confirming successful copper uptake. Fig. 4b exhibits the high-resolution Cu 2p spectra which further proves the presence of copper ions. Table S1 summarizes elemental composition changes from XPS analysis before and after copper adsorption. The Ca/P atomic ratio decreased from 1.34 (pre-adsorption) to 1.19 (post-adsorption), indicating ion exchange between Cu^{2+} and lattice Ca^{2+} during the adsorption process. Fig. 4c displays pH-dependent ζ-potential changes of the sample ET-70 in aqueous solutions. The surface charge exhibited significant variation across the pH range (3–7), transitioning from positive values at acidic conditions to negative values in alkaline media. The point of zero charge (PZC) occurred at pH 3.95, consistent with reported values for stoichiometric HA.[35] Below PZC, protonation of surface phosphate groups ($\equiv PO^- + H^+ \rightarrow \equiv POH$) generated net positive charges ($\zeta = +5.86$ mV at pH 3.0). Above the PZC, progressive deprotonation of calcium hydroxyl sites ($\equiv CaOH \rightarrow \equiv CaO^- + H^+$) and phosphate groups ($\equiv POH \rightarrow \equiv PO^- + H^+$) resulted in increasingly negative potentials, reaching $\zeta = -1.45$ mV at pH 5.0. Fig. 4d illustrates pH variations in post-adsorption solutions across different C_0 [Cu^{2+}]. At a fixed initial pH of 5.5: (1) For C_0 [Cu^{2+}] = 10 mg L^{-1}, the final pH increased to 5.66. This slight rise stems from preferential complexation of Cu^{2+} with deprotonated phosphate groups ($\equiv PO^-$), which liberates OH^- ions. (2) As C_0 [Cu^{2+}] increased from 20 to 200 mg L^{-1}, the final pH progressively decreased from 5.31 to 4.46. This reduction is attributed to Cu^{2+} complexation with calcium-coordinated hydroxyl groups ($\equiv$Ca–OH), releasing H^+ ions. Complemented by XPS analyses, these results confirm two dominant adsorption mechanisms: (1) ion exchange between lattice Ca^{2+} in HA and aqueous Cu^{2+}, (2) surface complexation where Cu^{2+} binds $\equiv$Ca–OH sites, accompanied by proton release.

In practice, during the adsorption process for the treatment of copper-contaminated water, the performance of the adsorbent is affected by the pH value of the water and the co-existing ions in the water. Fig. 5a shows the effect of pH on the copper removal efficiency of the sample ET-70, where the pH ranges

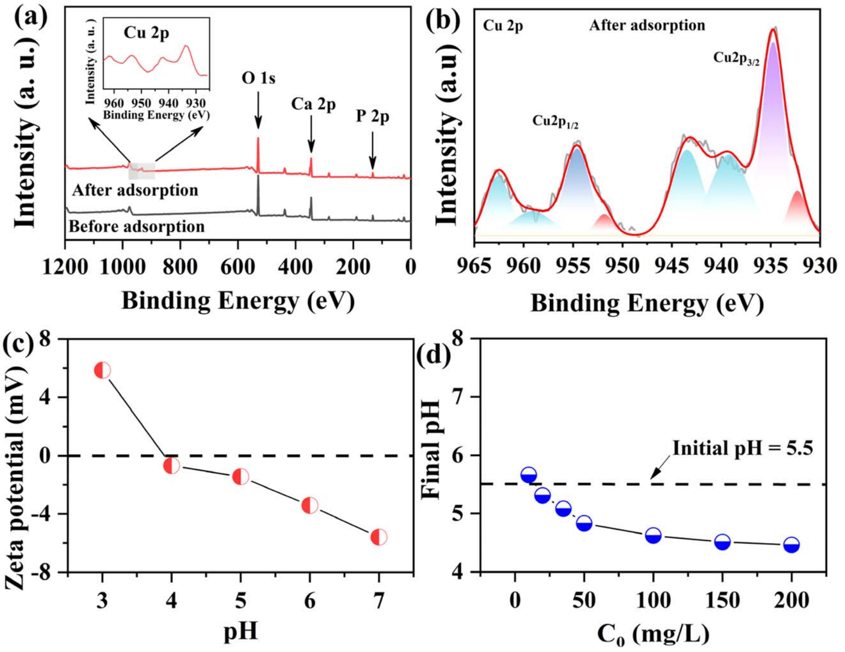

Fig. 4 (a) XPS spectra of the sample ET-70 before and after adsorption; (b) Cu 2p spectra of the sample ET-70 after adsorption; (c) ζ-potential of the sample ET-70 nanoparticles *versus* initial solution pH; (d) pH variation of the solution after copper adsorption.

from 3.0 to 5.5. Overall, the adsorption performance of all the samples increased as the pH increased from 3.0 to 5.5. The highest copper removal efficiency is achieved with 96.52% at pH 5.5. Besides, the copper removal efficiency could be maintained above 95% with wide pH range from 3.5 to 5.5. Fig. 5b shows the effect of coexisting ions on the copper removal performance of the sample ET-70. The removal of copper ions by the ET-70 was almost the same as that of the blank samples, which was around 95% in the studied concentration ranges of K^+, Na^+ and Mg^{2+} ions. When the Ca^{2+} ions concentration in the water was increased from 0 mM to 1.0 mM, the copper removal efficiency of sample ET-70 decreased from 92.82% to 89.62%. This indicates that there is competing effect on the solid surface between calcium ions and copper ions.

Fig. 6a shows the schematic of the membrane filtration setup comprising three main components: (a) feed reservoir containing unfiltered copper ion solution, (b) membrane filtration unit housing a circular hydroxyapatite nanowire membrane (diameter: 25 mm; mass: 0.03 g), and (c) collection vessel for filtered solution. Filtration was driven by a peristaltic pump to maintain controlled flow rates. Under specified experimental conditions (membrane thickness, flow rate, initial Cu^{2+} concentration), filtration experiments were conducted with filtrate concentration measured per 10-mL aliquot, enabling real-time removal efficiency calculation.

Fig. 6b and c shows the effect of initial copper concentration on the filtration performance of HA nanowire membranes. As the initial Cu^{2+} concentration increased from 5 to 7.5 and 10 mg L^{-1}, the removal efficiency for the first 10-mL filtrate decreased from 97.42% to 97.93% and 97.12%, respectively. Continuous filtration revealed progressive deterioration of performance: removal efficiency declined while filtrate Cu^{2+} concentration increased with cumulative volume. Using 2.0 mg L^{-1} as the safety threshold for effluent copper concentration according to WHO standards, the maximum safe throughput volumes reached 97.12 mL, 79.36 mL, and 53.91 mL

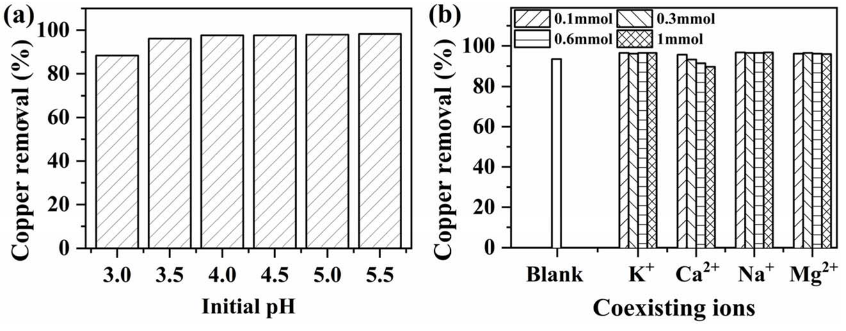

Fig. 5 Influence of initial solution pH (a) and coexisting ions (b) on the adsorption capacity of the sample ET-70. Experimental conditions: adsorbent dose = 0.4 g L^{-1}, temperature = 25 °C, adsorption time = 24 h, and C_0 = 10 mg L^{-1}.

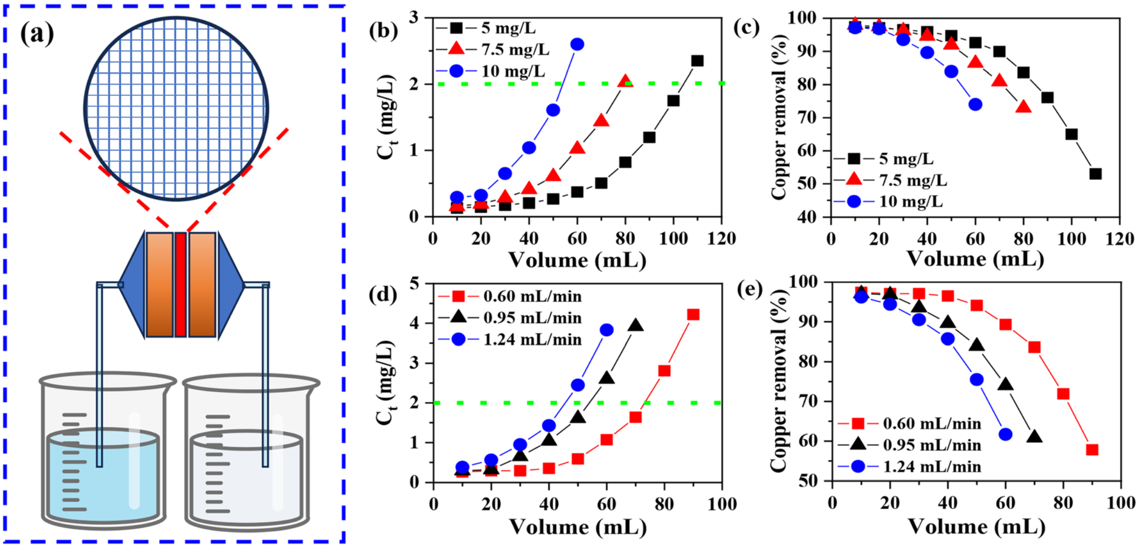

Fig. 6 Cu^{2+} removal performance of the HA nanowire membrane. (a) Schematic of the filtration setup. The equilibrium concentration (b) and removal efficiency (c) versus + the filtrate volume at different initial Cu^{2+} concentrations. Equilibrium concentration (d) and removal efficiency (e) as function of filtrate volume at different flow rates.

at initial concentrations of 5, 7.5, and 10 mg L^{-1}, respectively. Consequently, the copper removal capacity thresholds of HA nanowire membranes were calculated as 197.95, 161.75, and 109.88 L m^{-2}.

Fig. 6d and e shows the effect of flow rate on the filtration performance of HA nanowire membranes. As the initial Cu^{2+} concentration increased from 5 to 7.5 and 10 mL min^{-1}, the removal efficiency for the first 10-mL filtrate decreased from 97.42% to 97.12% and 96.22%, respectively. Continuous filtration revealed progressive deterioration of performance: removal efficiency declined while filtrate Cu^{2+} concentration increased with cumulative volume. The maximum safe throughput volumes reached 73.73 mL, 53.65 mL, and 44.97 mL at flow rate of 0.60, 0.95, and 1.24 mL min^{-1}, respectively. Consequently, the copper removal capacity thresholds of HA nanowire membranes were calculated as 150.28, 109.35, and 91.66 L m^{-2}.

4 Conclusion

In summary, the oleic acid capped HA nanowires can be effectively and rapidly removed with hot ethanol treatment, yielding HAP NWs with clean surfaces. These clean-surface HA nanowires exhibited significantly higher Cu^{2+} adsorption capacity compared to untreated nanowires. Batch adsorption experiments demonstrated that ET-70 achieved a Cu^{2+} adsorption capacity of 63.92 mg g^{-1} under conditions of an initial Cu^{2+} concentration of 200 mg L^{-1} and a temperature of 45 °C. The Cu^{2+} adsorption behavior of HA nanowires followed the Langmuir isotherm model and pseudo-second-order kinetic model. Remarkably, ET-70 maintained high Cu^{2+} removal efficiency across a wide pH range and in the presence of coexisting ions. Membrane filtration tests showed that a HA nanowires filter membrane with a thickness of 150 µm, operating at a flow rate of 0.95 mL min^{-1} and an influent Cu^{2+} concentration of 5 mg L^{-1}, achieved a treatment capacity of 197.95 liters per square meter, meeting the World Health Organization standard. The primary adsorption mechanism is attributed to ion exchange between Ca^{2+} in HA and Cu^{2+}, combined with complexation between surface hydroxyl groups and Cu^{2+}. Therefore, this study not only provides a simple and efficient method for obtaining clean HA nanowires surfaces to enhance their potential for subsequent functionalization and modification, but also establishes an experimental foundation for utilizing oleic acid-assisted hydrothermally synthesized HAP nanowires in membrane adsorption filtration for heavy metal ion removal from water.

Conflicts of interest

There are no conflicts to declare.

Data availability

The authors confirm that the data supporting the findings of this study are available within the article and/or its supplementary information (SI). Supplementary information is available. See DOI: https://doi.org/10.1039/d5ra06089c.

Acknowledgements

This work was financially supported by the Natural Science Foundation of Hubei Province (No. 2018CFB710), and Opening Fund of Hubei Provincial Key Laboratory of Green Materials for Light Industry (No. 202107B07), Hubei University of Technology.

References

1 M. Sadat-Shojai, M. T. Khorasani, E. Dinpanah-Khoshdargi and A. Jamshidi, Synthesis methods for nanosized

hydroxyapatite with diverse structures, *Acta Biomater.*, 2013, **9**, 7591–7621.

2 A. Szczes, L. Holysz and E. Chibowski, Synthesis of hydroxyapatite for biomedical applications, *Adv. Colloid Interface Sci.*, 2017, **249**, 321–330.

3 X. Zhou, Y. Qian, L. Chen, T. Li, X. Sun, X. Ma, J. Wang and C. He, Flowerbed-Inspired Biomimetic Scaffold with Rapid Internal Tissue Infiltration and Vascularization Capacity for Bone Repair, *ACS Nano*, 2023, **17**, 5140–5156.

4 D. Liu, W. Nie, D. Li, W. Wang, L. Zheng, J. Zhang, J. Zhang, C. Peng, X. Mo and C. He, 3D printed PCL/SrHA scaffold for enhanced bone regeneration, *Chem. Eng. J.*, 2019, **362**, 269–279.

5 M. Hatakeyama, H. Kishi, Y. Kita, K. Imai, K. Nishio, S. Karasawa, Y. Masaike, S. Sakamoto, A. Sandhu, A. Tanimoto, T. Gomi, E. Kohda, M. Abe and H. Handa, A two-step ligand exchange reaction generates highly water-dispersed magnetic nanoparticles for biomedical applications, *J. Mater. Chem.*, 2011, **21**, 5959–5966.

6 C. Heng, X. Zhou, X. Zheng, M. Liu, Y. Wen, H. Huang, D. Fan, J. Hui, X. Zhang and Y. Wei, Surface grafting of rare-earth ions doped hydroxyapatite nanorods (HAp:Ln(Eu/Tb)) with hydrophilic copolymers based on ligand exchange reaction: Biological imaging and cancer treatment, *Mater. Sci. Eng., C*, 2018, **91**, 556–563.

7 M. Ibrahim, M. Labaki, J. M. Giraudon and J. F. Lamonier, Hydroxyapatite, a multifunctional material for air, water and soil pollution control: A review, *J. Hazard. Mater.*, 2020, **383**, 121139.

8 X. Jin, X. Chen, Y. Cheng, L. Wang, B. Hu and J. Tan, Effects of hydrothermal temperature and time on hydrothermal synthesis of colloidal hydroxyapatite nanorods in the presence of sodium citrate, *J. Colloid Interface Sci.*, 2015, **450**, 151–158.

9 X. Jin, J. Zhuang, Z. Zhang, H. Guo and J. Tan, Hydrothermal synthesis of hydroxyapatite nanorods in the presence of sodium citrate and its aqueous colloidal stability evaluation in neutral pH, *J. Colloid Interface Sci.*, 2015, **443**, 125–130.

10 Y.-F. Shao, X. Qing, Y. Peng, H. Wang, Z. Shao and K.-Q. Zhang, Enhancement of mechanical and biological performance on hydroxyapatite/silk fibroin scaffolds facilitated by microwave-assisted mineralization strategy, *Colloids Surf., B*, 2021, **197**, 111401.

11 A. K. D. V. K. Wimalasiri, M. S. Fernando, G. R. Williams, D. P. Dissanayake, K. M. N. de Silva and R. M. de Silva, Microwave assisted accelerated fluoride adsorption by porous nanohydroxyapatite, *Mater. Chem. Phys.*, 2021, **257**, 123712.

12 H. Chen, R. Wang, L. Qian, H. Liu, J. Wang and M. Zhu, Surface modification of urchin-like serried hydroxyapatite with sol-gel method and its application in dental composites, *Composites, Part B*, 2020, **182**, 107621.

13 B. Q. Lu, Y. J. Zhu and F. Chen, Highly flexible and nonflammable inorganic hydroxyapatite paper, *Chemistry*, 2014, **20**, 1242–1246.

14 Z. C. Xiong, Y. J. Zhu, F. F. Chen, T. W. Sun and Y. Q. Shen, One-Step Synthesis of Silver Nanoparticle-Decorated Hydroxyapatite Nanowires for the Construction of Highly Flexible Free-Standing Paper with High Antibacterial Activity, *Chemistry*, 2016, **22**, 11224–11231.

15 J. Tan, Y. Liu, J. Gong, X. Jin, C. Cheng, R. Zhang and M. Chen, Non-aqueous liquid crystals of hydroxyapatite nanorods, *Acta Biomater.*, 2020, **116**, 383–390.

16 Y. Xu, X. Yan, H. Zhou, B. Wang and G. Shi, Tailoring Biotribological Performance of Polytetrafluoroethylene Nanocomposites through Control of Diameters and Aspect Ratios of In Situ Filled Hydroxyapatite Nanowires, *Adv. Eng. Mater.*, 2022, **25**, 2200943.

17 B. Cao, M. Yang, L. Wang, H. Xu, Y. Zhu and C. Mao, Cleaning" the Surface of Hydroxyapatite Nanorods by a Reaction-Dissolution Approach, *J. Mater. Chem. B*, 2015, **3**, 7667–7672.

18 T. Li, B. Wang, J. Ning, W. Li, G. Guo, D. Han, B. Xue, J. Zou, G. Wu, Y. Yang, A. Dong and D. Zhao, Self-Assembled Nanoparticle Supertubes as Robust Platform for Revealing Long-Term, Multiscale Lithiation Evolution, *Matter*, 2019, **1**, 976–987.

19 P. Das and N. R. Jana, Length-Controlled Synthesis of Calcium Phosphate Nanorod and Nanowire and Application in Intracellular Protein Delivery, *ACS Appl. Mater. Interfaces*, 2016, **8**, 8710–8720.

20 J. Tan, T. Pan, R. Su, M. Wang and Y. Jiang, Ultra-rapid transfer of oleic acid-coated hydroxyapatite nanocrystals into water via a sodium citrate-assisted ligand exchange strategy, *Colloids Surf. A Physicochem. Eng. Asp.*, 2023, **678**, 132464.

21 K. A. Lin, Y. T. Liu and S. Y. Chen, Adsorption of fluoride to UiO-66-NH2 in water: Stability, kinetic, isotherm and thermodynamic studies, *J. Colloid Interface Sci.*, 2016, **461**, 79–87.

22 J. P. Maity, C.-M. Hsu, T.-J. Lin, W.-C. Lee, P. Bhattacharya, J. Bundschuh and C.-Y. Chen, Removal of fluoride from water through bacterial-surfactin mediated novel hydroxyapatite nanoparticle and its efficiency assessment: Adsorption isotherm, adsorption kinetic and adsorption Thermodynamics, *Environ. Nanotechnol. Monit. Manag.*, 2018, **9**, 18–28.

23 Y. Chen, M. Li, Y. Li, Y. Liu, Y. Chen, H. Li, L. Li, F. Xu, H. Jiang and L. Chen, Hydroxyapatite modified sludge-based biochar for the adsorption of Cu2+ and Cd2+: Adsorption behavior and mechanisms, *Bioresour. Technol.*, 2021, **321**, 124413.

24 Z. Liu, J. Zhao, A. Wang, H. Yuan and Y. Chi, Adsorption behavior and mechanism of Cu(II) by sodium alginate/carboxymethylcellulose/magnesium hydroxide (SC-MH) hydrogel, *Int. J. Biol. Macromol.*, 2024, **277**, 134046.

25 M. Jimenez-Reyes and M. Solache-Rios, Sorption behavior of fluoride ions from aqueous solutions by hydroxyapatite, *J. Hazard. Mater.*, 2010, **180**, 297–302.

26 L. Yang, Z. Wei, W. Zhong, J. Cui and W. Wei, Modifying hydroxyapatite nanoparticles with humic acid for highly

efficient removal of Cu(II) from aqueous solution, *Colloids Surf. A Physicochem. Eng. Asp.*, 2016, **490**, 9–21.

27 K.-W. Jung, S. Y. Lee, J.-W. Choi and Y. J. Lee, A facile one-pot hydrothermal synthesis of hydroxyapatite/biochar nanocomposites: Adsorption behavior and mechanisms for the removal of copper(II) from aqueous media, *Chem. Eng. J.*, 2019, **369**, 529–541.

28 J. Zhang, X. Xia, K. Li, Y. Shen and Y. Xue, New insights into temperature-induced mechanisms of copper adsorption enhancement on hydroxyapatite-in situ self-doped fluffy bread-like biochar, *Chem. Eng. J.*, 2024, **479**, 147657.

29 L. Deng, Y. Li, A. Zhang and H. Zhang, Nano-hydroxyapatite incorporated gelatin/zein nanofibrous membranes: Fabrication, characterization and copper adsorption, *Int. J. Biol. Macromol.*, 2020, **154**, 1478–1489.

30 J. Guo, Y. Han, Y. Mao and M. N. Wickramaratne, Influence of alginate fixation on the adsorption capacity of hydroxyapatite nanocrystals to Cu2+ ions, *Colloids Surf. A Physicochem. Eng. Asp.*, 2017, **529**, 801–807.

31 X. Liu, H. Yin, H. Liu, Y. Cai, X. Qi and Z. Dang, Multicomponent adsorption of heavy metals onto biogenic hydroxyapatite: Surface functional groups and inorganic mineral facilitating stable adsorption of Pb(II), *J. Hazard. Mater.*, 2023, **443**, 130167.

32 L. Shi, Z. Zhu, N. Wu, Y. Chang, L. Yue and L. An, Natural hydroxyapatite powder from pig-bone waste (pHAP) for the rapid adsorption of heavy metals (Cu) in aqueous solution, *Adsorption*, 2024, **30**, 801–812.

33 H. Hernández-Cocoletzi, R. A. Salinas, E. Águila-Almanza, E. Rubio-Rosas, W. S. Chai, K. W. Chew, C. Mariscal-Hernández and P. L. Show, Natural hydroxyapatite from fishbone waste for the rapid adsorption of heavy metals of aqueous effluent, *Environ. Technol. Innovat.*, 2020, **20**, 101109.

34 Y. Liu, Y. Yan, B. Seshadri, F. Qi, Y. Xu, N. Bolan, F. Zheng, X. Sun, W. Han and L. Wang, Immobilization of lead and copper in aqueous solution and soil using hydroxyapatite derived from flue gas desulphurization gypsum, *J. Geochem. Explor.*, 2018, **184**, 239–246.

35 I. D. Smičiklas, S. K. Milonjić, P. Pfendt and S. Raičević, The point of zero charge and sorption of cadmium (II) and strontium (II) ions on synthetic hydroxyapatite, *Sep. Purif. Technol.*, 2000, **18**, 185–194.